

Automatic Landslide Mapping From Satellite Imagery With a Topography-Driven Thresholding Algorithm

Massimiliano Alvioli, Alessandro C. Mondini, Federica Fiorucci, Mauro Cardinali, and Ivan Marchesini

Istituto di Ricerca per la Protezione Idrogeologica, Consiglio Nazionale delle Ricerche, via Madonna Alta 126, I-06128, Perugia, Italy

Corresponding author:

Massimiliano Alvioli

Email address: massimiliano.alvioli@irpi.cnr.it

ABSTRACT

We present an improvement of image classification for landslide mapping by “thresholding”, using topographic information to determine multiple thresholds. We devised a two-steps procedure for automatic classification into landslide or no landslide categories of a change-detection map obtained from satellite imagery. Requirements of the proposed procedure are knowledge of the occurrence of a landslide event, availability of a pre- and post- event pseudo-sereo image pair and a digital elevation model. The novel feature of the approach is represented by the use of slope units as topographic-aware subsets of the scene within which we apply a multiple thresholding method to classify a landslide class membership tuned on the sole landslide spectral response. The method is fully automatic after site-dependent operations, required only once, are performed, and exhibits improved classification performance with limited training requirements. Our automatic procedure is a step forward towards systematic acquisition of landslide events and real-time landslide mapping from satellite imagery.

INTRODUCTION

The most effective source of information describing a landslide event extension and magnitude in a given region is an event landslide inventory map (eLIM). An eLIM is a key input to derive landslide hazard and risk maps, and its preparation require effective monitoring and fast, cost-efficient mapping tools. More in general, despite their importance, landslide inventory maps cover a limited extension of the landslide-prone areas across the global landmass (Guzzetti et al., 2012; Marchesini et al., 2014).

Landslide inventory maps are best prepared by visual interpretation of stereoscopic aerial images (Fiorucci et al., 2011). In the last two decades the images captured by high resolution and very high resolution optical satellites (Guzzetti et al., 2012; Casagli et al., 2017), and synthetic aperture radar (Casagli et al., 2017; Mondini, 2017), are becoming a viable replacement of aerial photographs, encouraging research efforts in the direction of developing automatic and semi-automatic classification algorithms to distinguish different land covers, including vegetation, urban areas, water bodies and landslides. Use of LiDAR data for automatic landslide mapping is beyond the scope of this work, mainly because it is not suitable for use within the approach described here, and will not be discussed.

Automatic and semi-automatic landslide mapping require image classification methods, including supervised and unsupervised clustering (Borghuis et al., 2007; Martha et al., 2011), and index thresholding (Rosin and Hervás, 2005; Alvioli et al., 2018). Supervised classification calls for a manual training process which can result difficult and time consuming. Reducing the time and the overall effort required to prepare an eLIM, while increasing the level of automation of the mapping procedure, are key issues to obtain a reliable estimate of the extent and magnitude of landslide events on a routinely basis.

In this work, we focus on a classification method which assigns individual pixels to the generic bare soil class, with a spectral fingerprint corresponding to landslides (Mondini and tsung Chang, 2014) occurred within an individual event. We use a Bayesian-based maximum likelihood (ML) approach

46 to assign each pixel either to the “landslide” or “no landslide” land cover classes by thresholding, the
47 simplest existing decision rule. The procedure requires to single out a numerical value (threshold), among
48 all the values in the image, and to assign the pixels values above (or below) the threshold to a particular
49 class (Cheng et al., 2004). We used thresholding to classify a change detection (CD) function, obtained
50 from a combination of widely used change detection indices tuned on landslide spectral response. In
51 particular, we devised a multi-threshold approach that takes advantage of the topographic information
52 contained in a slope unit (SU) subdivision of the area under investigation (Carrara, 1993; Guzzetti et al.,
53 1999; Alvioli et al., 2016; Schlägel et al., 2018; Bornetxea et al., 2018). Slope units are morphological
54 terrain units bounded by drainage and divide lines, and corresponds to what a geomorphologist or a
55 hydrologist would recognize as single slopes, a combination of adjacent slopes, or small catchments.

56 Using a custom classification threshold within each slope unit allows to overcome limitations posed
57 by the different geometric conditions, dictated by the combination of satellite point of view, sun position,
58 slope orientation and inclination (Fiorucci et al., 2018a). Such conditions can be considered homogeneous
59 within typical individual SUs, while they pose limitations when the CD function values are classified
60 using a single threshold. A large number of false negatives and false positives are inherently introduced
61 by a single threshold. On the other hand, misclassifications may be strongly reduced using multiple
62 thresholds.

63 METHODS AND RESULTS

64 Our method to automatically identify the pixels belonging to the landslide land cover class relies on the
65 concept of a CD function, denoted here and in Alvioli et al. (2018) as g_{ls} (“ls” stands for “landslides”),
66 obtained with a simplified ML classifier. Figure 1 summarizes the method developed in Alvioli et al.
67 (2018), illustrating the two basic steps, which we updated in this work.

68 In the first step, we define the function g_{ls} whose values represent the ML distance of each pixel
69 from the landslide class, providing a pixel-by-pixel measure of the presence or absence of new landslides.
70 The g_{ls} function is obtained measuring changes occurred between a pre- and a post-event image, using
71 three different metrics: changes of NDVI (Tucker, 1979), Spectral Angle (SA) (Sohn and Rebello, 2002;
72 Richards and Jia, 2006; Mondini et al., 2011b) and Principal Component Analysis (PCA) (Richards and
73 Jia, 2006). The three metrics were combined in a single image stack of changes for the analysis.

74 In the second step, a map is generated by evaluating the g_{ls} function in each pixel of the study area.
75 Then the g_{ls} map pixels are classified as “landslide” or “no landslide”, either by: (i) thresholding the
76 g_{ls} values, i.e., selecting as landslides the pixels with g_{ls} values larger than a single threshold value over
77 the whole study area; (ii) using multiple threshold values, within square and rectangular subsets of the
78 g_{ls} map; (iii) as in (ii), but replacing regular subsets with irregular SU polygons, thus introducing local
79 geomorphological information.

80 In the first step, the innovative feature is represented by the fact that we only aim at defining the
81 landslide class, thus we only need to train the procedure once. In the test case of Alvioli et al. (2018), the
82 calibration area was selected in only one (big) landslide, for a total of 421 pixels (about 10,000 m² out of
83 about 1,000 km²) in the stack of changes.

84 In the second step, the core innovation of the procedure is the application of thresholding g_{ls} values
85 within a large number of subsets of the study area, singled out either with and without a topographic
86 information. Existing thresholding approaches use a single threshold, necessarily reducing accuracy,
87 while SU provide local topography information and allows to find local custom thresholds.

88 The proposed method was tested in an area of about 1,000 m² in Myanmar, where torrential rainfall
89 triggered extensive landslides in 2015, including the massive Tonzang landslide and the large number of
90 fatalities (Brakenridge et al., 2017).

91 Figure 2 shows histograms of the values for the CD discriminant function g_{ls} . A distinctive feature of
92 the global histogram, Figure 2(a), is a bi-modal behavior, characterized by a small peak around $g_{ls} = 0$,
93 overwhelmed by a broad peak containing the vast majority of pixels with spectral properties dissimilar
94 from the landslide ones. The two peaks (modes) are separated by a well-defined local minimum, occurring
95 at some g_{ls} value denoted as M. The first approximation to a binary classification of the g_{ls} values is to
96 flag as “landslide” the pixels with $M < g_{ls} < 0$, and to flag as “no-landslide” the remaining pixels.

97 The next approximation we discuss consists in tracing a grid onto the g_{ls} map, calculate a histogram
98 of the values of g_{ls} for each rectangular polygon singled out by the grid, and process the histogram with
99 the automatic, non-parametric mode detection software of Delon et al. (2007), implemented as standalone

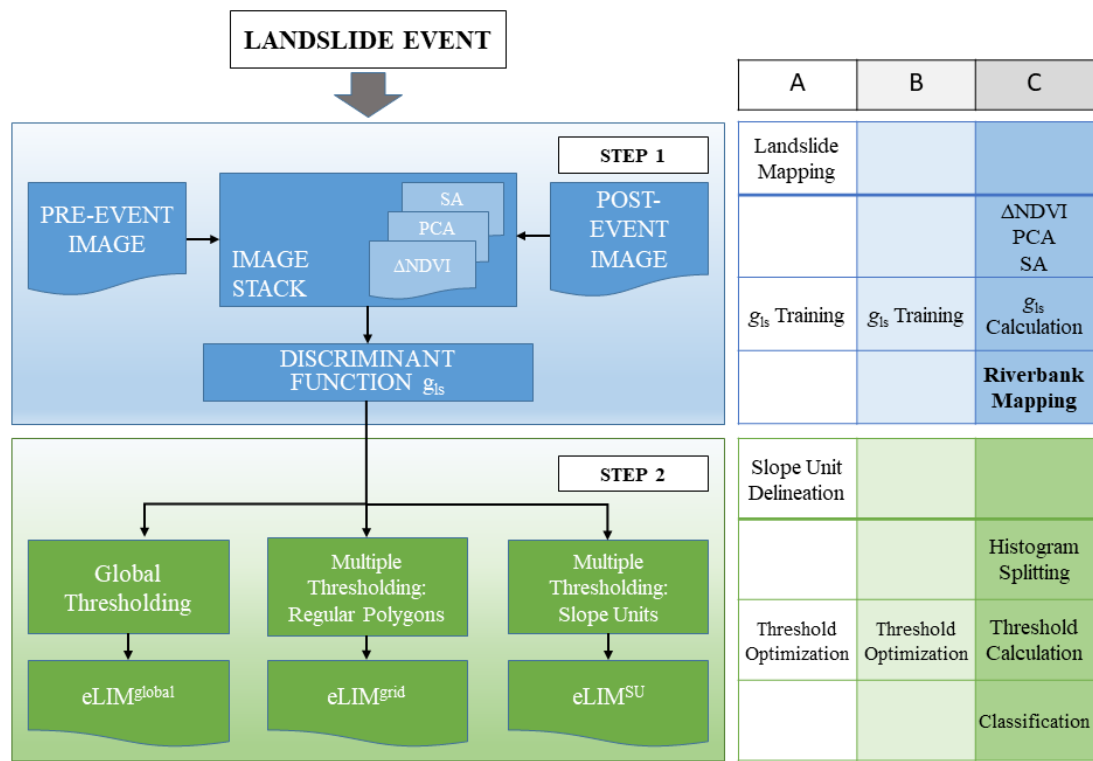


Figure 1. The algorithm proposed in Alvioli et al. (2018), and updated in this work, applied upon knowledge of the occurrence of a landslide event. Step 1: calculation of the discriminant function; step 2: three different classification possibilities by index thresholding, resulting in three different eLIMs (cf. Section II). The table describes the level of automation of the individual operations involved in each of the two steps. A: one-time, site-dependent operations; B: operations that can be optionally performed again in a new study area; C: fully automatic operations, to which we added “Riverbank Mapping” in this work, with respect to Alvioli et al. (2018).

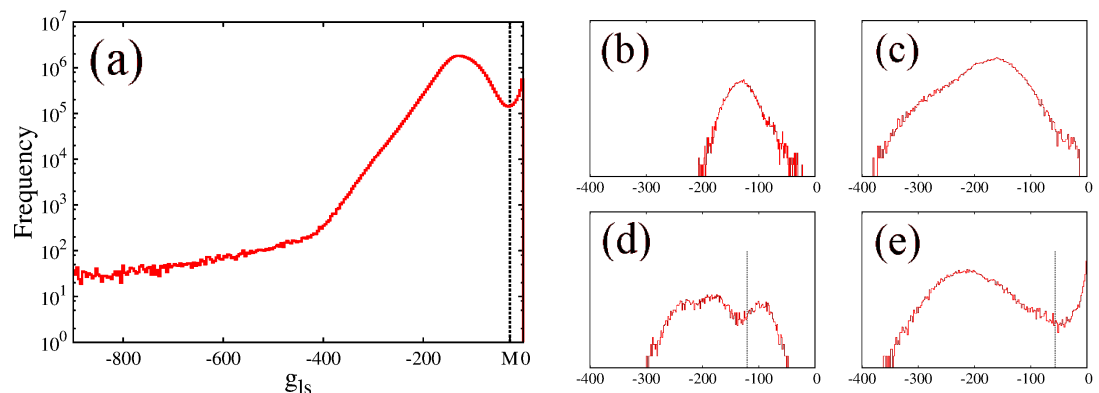


Figure 2. (a): histogram of the g_{ls} function values over the whole study area. (b-d): four sample histograms of the g_{ls} values, corresponding to four individual slope units. The vertical lines represent the divide between different modes of the distributions, if more than one exist. The mode located right from the divide may be due (e), or may not be due (d), to pixels with spectral behavior very similar to pixels known to be within the landslides selected for the training procedure, by construction of g_{ls} .

100 program. Depending on the number and values of the separations between different modes found by
101 the software, we developed an algorithm to determine custom thresholds to be applied within the single
102 polygons we introduced.

103 The third and last approximation is to replace the rectangular polygons with topography-aware slope
104 units. Figure 2(b)-(e) shows a sample of the resulting histograms, with the corresponding separations
105 between different modes of the distributions. The histograms of Figure 2(b)-(c) only have one mode, thus
106 zero separations; the histograms of Figure 2(d)-(e) have two modes, and one separation.

107 SU were delineated using the automatic software of Alvioli et al. (2016), using a portion of ASTER
108 digital elevation model, and are shown in Figure 3 for the calibration study area (about 1/4 in size of
109 the whole area). The number and size of SU were chosen maximizing agreement of the automatic
110 classification with an eLIM prepared by expert geomorphologists, by photo-interpretation, in a calibration
111 region. The method was then extended to a different, and wider, validation region. Visual interpretation
112 and g_{ls} analysis were performed on a 5m x 5m RapidEye stereo-pair.

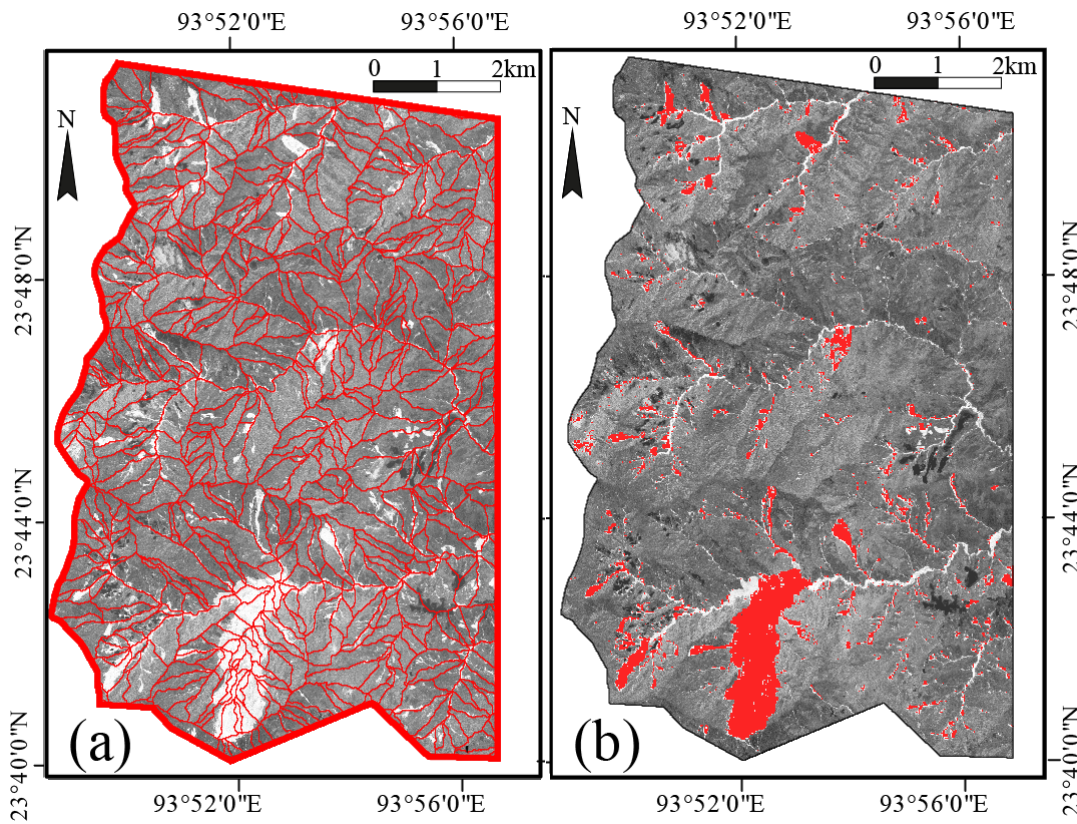


Figure 3. (a): the SU subdivision of the calibration area, in the calibration subset of our test area located in Myanmar (see Alvioli et al. (2018) for details). (b): red pixels denote the automatically-mapped landslide inventory, $eLIM^{SU}$ (cf. Figure 1), obtained with multiple thresholds within the SU polygons shown in (a).

113 In this work, we added an additional level of automation with respect to the work in Alvioli et al.
114 (2018). The comparison between automatic and expert mapping was performed everywhere but on
115 pixels corresponding to rivers. We automated riverbanks mapping using a pixel-based method (Mondini
116 and tsung Chang, 2014; Mondini et al., 2017), thus making the overall method fully automatic after
117 site-dependent operations, required only once, are performed. Such operations are listed in Fig. 1.

118 We report results of the three different approximations (also reported in Alvioli et al. (2018)), expressed
119 in terms of an error index E_I , first introduced in Carrara (1993) and recently employed as a benchmark
120 for selecting optimal requirements of images from remote sensing for landslide mapping (Fiorucci et al.,
121 2018b). Results for “grid” and “SU” are obtained with a number of polygons that minimizes E_I in both
122 cases. Results are listed in Table I. The percentage gain of multi-thresholding with respect to the “global”,

123 single-threshold results, are calculated as $(E_I^{SU} - E_I^{global})/E_I^{global}$, in the SU case, and correspond to 8.1%
124 in training and 4.8% in validation.

125 Eventually, we replaced riverbanks mapped by visual interpretation with a riverbank layer mapped
126 automatically and calculated E_I in the training area using the new layer; results are listed in Table I as
127 well. The percentage gain using SUs (7.7%) is comparable to the results obtained with visual mapping of
128 riverbanks (8.1%).

129 DISCUSSION AND CONCLUSIONS

130 The topography-driven, multi-threshold approach to landslide mapping from satellite imagery proposed
131 in Alvioli et al. (2018), and updated in this work, presents several advantages.

132 The numerical results of the comparison of the automatic mapping procedure with the ground-truth of
133 an eLIM prepared by visual interpretation (Table I) reveal that the topographic-aware subdivision of the
134 territory allows for a better classification performance both than thresholding applied globally, or within
135 a topographic-blind subdivision. This is particularly true in the validation area, where the grid-based
136 method shows little gain (0.4%) with respect to the global thresholding method.

137 In second place, we substantially simplified image preparation with respect to existing land cover
138 classification methods using remote sensing. Considering the only “landslide” class reduces the time and
139 effort needed to train the algorithm to distinguish the spectral response of landslides.

140 In third place, once the preliminary steps of SU delineation, g_{ls} training and calibration of thresholds
141 are performed, the procedure is fully automatic, including the detection of riverbanks, left out of our
142 previous work (Alvioli et al., 2018). Class assignment is automatic and it does not require a-posteriori
143 identification of the different classes. Figure 1 contains a table describing the different levels of automation
144 of the various actions required to achieve multi-threshold classification.

145 In preparing the g_{ls} function map, we combined three indices embodying both radiometric (Δ NDVI
146 and SA) and geometric (PCA) information contained in satellite images, to account for the heterogeneity
147 showed by the spectral response of landslides (Mondini et al., 2011b,a). Further developments may
148 include different indices, in the discriminant function preparation, or additional topographic drivers
149 (Blaschke et al., 2014). The method can be used on a routinely basis, and run whenever the occurrence
150 of a new landslide event is otherwise detected with specialized methods (Mondini, 2017; Mondini et al.,
151 2017).

152 In conclusion, we argue that the improved performance and limited training requirements of the
153 classification procedure represent a step forward towards an automatic, reliable real-time landslide
154 mapping from satellite imagery.

Riverbanks Mapping	Training				Validation		
	E_I	0.369	0.344	0.399	0.512	0.510	0.487
Visual	Gain	–	6.7%	8.1%	–	0.4%	4.8%
	E_I	0.401	–	0.370	–	–	–
Automatic	Gain	–	–	7.7%	–	–	–

155 **Table 1.** Numerical results from the comparison of eLIMs obtained with global thresholding and with
grid-based and SU-based multi-threshold presented in this work and Alvioli et al. (2018).

155 ACKNOWLEDGMENTS

156 Partial support for this work was provided by the Natural Environment Research Council (NERC) [grant
157 number NERC/DFID NE/P000681/1], within the LANDSLIP project¹.

1¹<http://www.landslip.org>

158 REFERENCES

- 159 Alvioli, M., Marchesini, I., Reichenbach, P., Rossi, M., Ardizzone, F., Fiorucci, F., and Guzzetti, F. (2016).
160 Automatic delineation of geomorphological slope-units with r.slopeunits v1.0 and their optimization
161 for landslide susceptibility modeling. *Geoscientific Model Development*, 9:3975–3991.
- 162 Alvioli, M., Mondini, A. C., Fiorucci, F., Cardinali, M., and Marchesini, I. (2018). Topography-driven
163 satellite imagery analysis for landslide mapping. *Geomatics, Natural Hazards and Risk*, 9(1):544–567.
- 164 Blaschke, T., Feizizadeh, B., and Hölbling, D. (2014). Object-based image analysis and digital terrain
165 analysis for locating landslides in the urmia lake basin, iran. *IEEE Journal of Selected Topics in Applied
166 Earth Observations and Remote Sensing*, 7(12):4806–4817.
- 167 Borghuis, A. M., Chang, K., and Y., L. H. (2007). Comparison between automated and manual mapping
168 of typhoon triggered landslides from SPOT 5 imagery. *International Journal of Remote Sensing*, 28(8).
- 169 Bornaeux, T., Rossi, M., Marchesini, I., and Alvioli, M. (2018). Effective surveyed area and its
170 role in statistical landslide susceptibility assessments. *Natural Hazards and Earth System Sciences*,
171 18(9):2455–2469.
- 172 Brakenridge, G., Syvitski, J., Niebuhr, E., Overeem, I., Higgins, S., Kettner, A., and Prades, L. (2017).
173 Design with nature: Causation and avoidance of catastrophic flooding, Myanmar. *Earth-Science
174 Reviews*, 165(Supplement C):81 – 109.
- 175 Carrara, A. (1993). Uncertainty in evaluating landslide hazard and risk. In Nemec, J., Nigg, J. M., and
176 Siccardi, F., editors, *Prediction and Perception of Natural Hazards: Proceedings Symposium, 22–26
177 October 1990, Perugia, Italy*, pages 101–109, Dordrecht. Springer Netherlands.
- 178 Casagli, N., Frodella, W., Morelli, S., Tofani, V., Ciampalini, A., Intrieri, E., Raspini, F., Rossi, G., Tanteri,
179 L., and Lu, P. (2017). Spaceborne, UAV and ground-based remote sensing techniques for landslide
180 mapping, monitoring and early warning. *Geoenvironmental Disasters*, 4(1):9.
- 181 Cheng, K., Wei, C., and Chang, S. (2004). Locating landslides using multi-temporal satellite images.
182 *Advances in Space Research*, 33(3):296 – 301. Monitoring of Changes Related to Natural and Manmade
183 Hazards Using Space Technology.
- 184 Delon, J., Desolneux, A., Lisani, J. L., and Petro, A. B. (2007). A nonparametric approach for histogram
185 segmentation. *IEEE Transactions on Image Processing*, 16(1):253–261.
- 186 Fiorucci, F., Ardizzone, F., Mondini, A. C., Viero, A., and Guzzetti, F. (2018a). Visual interpretation of
187 stereoscopic NDVI satellite images to map rainfall-induced landslides. *Landslides*, pages 1–10.
- 188 Fiorucci, F., Cardinali, M., Carlà, R., Rossi, M., Mondini, A., Santurri, L., Ardizzone, F., and Guzzetti, F.
189 (2011). Seasonal landslide mapping and estimation of landslide mobilization rates using aerial and
190 satellite images. *Geomorphology*, 129(1–2):59 – 70.
- 191 Fiorucci, F., Giordan, D., Santangelo, M., Dutto, F., Rossi, M., and Guzzetti, F. (2018b). Criteria for
192 the optimal selection of remote sensing images to map event landslides. *Natural Hazards and Earth
193 System Sciences*, 18:405–417.
- 194 Guzzetti, F., Carrara, A., Cardinali, M., and Reichenbach, P. (1999). Landslide hazard evaluation: a
195 review of current techniques and their application in a multi-scale study, Central Italy. *Geomorphology*,
196 31(1):181 – 216.
- 197 Guzzetti, F., Mondini, A. C., Cardinali, M., Fiorucci, F., Santangelo, M., and Chang, K.-T. (2012).
198 Landslide inventory maps: New tools for an old problem. *Earth-Science Reviews*, 112(1–2):42 – 66.
- 199 Marchesini, I., Ardizzone, F., Alvioli, M., Rossi, M., and Guzzetti, F. (2014). Non-susceptible landslide
200 areas in Italy and in the Mediterranean region. *Natural Hazards and Earth System Sciences*, 14(8):2215–
201 2231.
- 202 Martha, T. R., Kerle, N., van Westen, C. J., Jetten, V., and Kumar, K. V. (2011). Segment optimization
203 and data-driven thresholding for knowledge-based landslide detection by object-based image analysis.
204 *IEEE Transactions on Geoscience and Remote Sensing*, 49(12):4928–4943.
- 205 Mondini, A. C. (2017). Measures of spatial autocorrelation changes in multitemporal SAR images for
206 event landslides detection. *Remote Sensing*, 9(6).
- 207 Mondini, A. C., Chang, K.-T., Chiang, S.-H., Schlögel, R., Notarnicola, C., and Saito, H. (2017). Auto-
208 matic mapping of event landslides at basin scale in Taiwan using a Montecarlo approach and synthetic
209 land cover fingerprints. *International Journal of Applied Earth Observation and Geoinformation*,
210 63:112 – 121.
- 211 Mondini, A. C., Guzzetti, F., Reichenbach, P., Rossi, M., Cardinali, M., and Ardizzone, F. (2011a).
212 Semi-automatic recognition and mapping of rainfall induced shallow landslides using optical satellite

- 213 images. *Remote Sensing of Environment*, 115(7):1743 – 1757.
- 214 Mondini, A. C. and tsung Chang, K. (2014). Combining spectral and geoenvironmental information for
215 probabilistic event landslide mapping. *Geomorphology*, 213:183 – 189.
- 216 Mondini, A. C., Tsung Chang, K., and Yuan Yin, H. (2011b). Combining multiple change detection
217 indices for mapping landslides triggered by typhoons. *Geomorphology*, 134(3–4):440 – 451.
- 218 Richards, J. and Jia, X. (2006). *Remote Sensing digital Image Analysis*. Springer-Verlag Berlin Heidelberg.
- 219 Rosin, P. L. and Hervás, J. (2005). Remote sensing image thresholding methods for determining landslide
220 activity. *International Journal of Remote Sensing*, 26(6):1075–1092.
- 221 Schlägel, R., Marchesini, I., Alvioli, M., Reichenbach, P., Rossi, M., and Malet, J.-P. (2018). Optimizing
222 landslide susceptibility zonation: Effects of DEM spatial resolution and slope unit delineation on
223 logistic regression models. *Geomorphology*, 301:10 – 20.
- 224 Sohn, Y. and Rebello, N. (2002). Supervised and unsupervised spectral angle classifiers. *Photogrammetric
225 Engineering and Remote Sensing*, 68(12):1271–1280. cited By 74.
- 226 Tucker, C. J. (1979). Red and photographic infrared linear combinations for monitoring vegetation.
227 *Remote Sensing of Environment*, 8(2):127 – 150.